terials, the po
promising m
suitable ener

the CH_4 evolution rate of CN/Sn_2S_3-DETA heterostructure catalyst is obviously higher than that of CN [27]. Besides, the CN/Bi_2MoO_6 heterojunction facilitated the separation and transfer of photogenetrated carriers, showing a higher photocatalytic H_2 production performance than CN under visible-light irradiation [30]. However, there are some differences of lattice matching among different semiconductors for these CN heterojunction materials, which affects the transmission and separation of photoinduced carriers from the heterojunction interface to a certain extent.

Our research have shown that the conduction band (CB), valence band (VB) of CNI is −1.13 eV, +1.53 eV versus Normal Hydrogen Electrode (NHE), respectively, and there is a very good band structure matching between CN (CB, VB is −0.92 eV and + 1.78 eV, respectively) and CNI. Obviously, extremely matched band structure offers a vital chance to fabricate CN/CNI homojunction semiconductors.

Herein, making full use of the topology-induced band offset and the almost same characteristics of lattice matching, electronic affinity and work function between CN and CNI, a novel CN/CNI homojunction catalyst was fabricated by a facile synthetic route. Compared with CN or CNI, the photocatalytic performance of CN/CNI catalyst was greatly improved under visible-light irradiation. In particular, the CN/CNI-40% catalyst with an optimized CN content indicated an excellent photocatalytic property, and its degradation ratio for RhB, H_2 evolution rate, CO_2 reduction rate is respectively 3.0, 2.2, 3.6 time higher than that of CNI-R (reference sample) with the highest photocatalytic activity in the literature (Adv. Mater. 2014, 26, 805–809). This study provides a facile strategy to fabricate stable, cheap and highly active multifunctional materials.

2. Experiments

2.1. Synthesis of catalysts

Synthesis process for one-step calcination of iodine-doped CN (CNI-O) is as follows. 2.0 g dicyandiamide and 1.0 g ammonium iodine were mixed by 15 mL deionized water with stirring, evaporating water molecules at 80 °C, then CNI-O precursors were calcined by a muffle furnace at 823 K reaction for 4.0 h. For comparative study, an iodine-doped CN reference sample (CNI-R) with the highest activity in the literature (Adv. Mater. 2014, 26, 805–809) [22] was also synthesized. Pure CN was obtained by the same way at the absence of ammonium iodine.

The CN/CNI catalysts were synthesized by mixing and sintering CNI-O (2.0 g) with different amounts of dicyandiamide. For example, CN/CNI-20% was obtained by grinding the mixture of CNI-O (2.0 g) and dicyandiamide (0.2 g) for 0.5 h, and subsequently calcined at 823 K reaction for 4.0 h to yield final catalyst. The other CN/CNI catalysts were also prepared by the same method, using 0.4 g or 0.6 g of dicyandiamide, and denoted as CN/CNI-40% and CN/CNI-60%, respectively. CNI (CNI-T) was obtained by secondary calcination of CNI-O at 823 K reaction for 4.0 h. Based on our previous research, 0.4 g dicyandiamide at 823 K reaction for 4.0 h can produce 0.1 g CN. Therefore, CN/CNI-40% (physical mixture) was obtained by grinding the mixture of CNI (2.0 g) and CN (0.1 g) for 1.0 h.

2.2. Characterizations

Fourier transformation infrared spectroscopy was measured on a Bruker Equinox 55 spectrometer with KBr pellets in the 500–3000 cm^{-1} region. Scanning electron microscopy was measured by Carl Zeiss Sigma 500. The characterization processes of valence band X-ray photoelectron spectroscopy, X-ray powder diffraction, UV–Vis diffuse reflectance spectra, X-ray photoelectron spectroscopy, photoluminescence and photoelectrochemistry reference to this document [22,23].

2.3. Activity measurements

The activities of catalysts were evaluated by the photocatalytic degradation of Rhodamine B (RhB) (60 mL, 10 mg/L) solution, and 300 W Xe lamp (λ > 420 nm) was used as light source and the amount of photocatalyst was 0.1 g. To ensure the adsorption equilibrium of solution and catalyst, the mixed solution was magnetically stirred for 0.5 h before illumination. About 4.0 mL mixed solution was extracted and centrifuged at fixed time, and then was analyzed by a TU-1901 spectroscopy. The change of total organic carbon (TOC) in the CN, CNI, CNI-R, CN/CNI-40% catalytic system was measured via a TOC (Shimadzu TOC-L CSH) monitoring system.

The evaluation of photocatalytic H_2 evolution references to this document [23]. The photocatalytic reduction of carbon dioxide (CO_2) into CH_4 reaction was performed in a Pyrex glass vessel, and Pt loading on catalysts was prepared by a photo-deposition method [34]. Then, 50 mg disperse catalyst was located at the bottom of a Pyrex glass cell, connecting with a closed system. The reaction system volume is ~230 mL. The reaction setup was vacuum-treated after several times, CO_2 gas with high purity was followed into the reaction setup to reach an ambient pressure. And then, 2.0 mL H_2O was injected into the reactor by a liquid syringe. Next, the reactor was stored under dark for 2.0 h, to reach the adsorption-desorption equilibrium. Finally, the reaction was irradiated by a 300 W Xe lamp (λ > 420 nm). At a given interval, from the reaction cell, 0.5 mL gaseous product was continually extracted, in order to check the concentration of CH_4 by using a gas chromatograph (Shimadzu, GC-2014, Ar carrier) during irradiation.

3. Results and discussion

3.1. Characterization

X-ray diffraction (XRD) results in Fig. 1A confirmed that CN, CNI, CN/CNI catalysts were crystalline and consisted of a typical graphite-like structure of CN, which was indicated by the diffraction peaks at 2θ angles of 27.4° and 13.0°, corresponding to the (002) and (100) crystal faces of layered CN [35,36]. At 27.4° and 13.0°, there was a strong and weak diffraction peak, were indexed to the inter-layer stacking and in-plane structural packing of conjugated aromatic systems, respectively [37]. It was found that no other diffraction peak was observed among CN, CNI and CN/CNI catalysts.

The functional group and structure of CNI, CN, CN/CNI catalysts were studied by fourier transformation infrared (FTIR) spectroscopy, and the results were shown in Fig. 1B. The absorption bands of these catalysts were found at about 805 and 1200–1700 cm^{-1}, belonging to the tri-s-triazine units and the aromatic C—N heterocycles of CN [38,39]. These FTIR results, together with the XRD analyses, indicated that the crystalline structure of CN was not changed after iodine doped.

The morphology of the CN, CNI and CN/CNI-40% catalysts was studied by scanning electron microscopy (SEM). As depicted in Fig. 2a, pure CN exhibited a large number of aggregated thick layers structures. Compared with CN, more micro-pores of small diameter size were observed on CNI surface (Fig. 2b). This change in microstructure probably was a result of NH_3 release by pyrolysis, which was induced by a sufficient doped with iodine at CN surfaces [22,23]. As described in Fig. 2c, after introducing CN, the CN/CNI-40% catalyst showed integrated morphology of pure CN and CNI together, suggesting the formation of CN/CNI homojunction catalyst. The element mapping images of the corresponding region shown in Fig. 2d, e, and f can further prove that the CN and CNI were coexistent and nearly homogeneously distributed in the CN/CNI-40% catalyst.

X-ray photoelectron spectroscopy (XPS) was used to reveal the surface component and interaction between CNI and CN in their homojunction catalysts. Fig. 3 depicted the XPS profiles of CNI, CN and CN/CNI-40% catalysts, where carbon (C) and nitrogen (N) elements were observed in these catalysts and iodine (I) element was detected

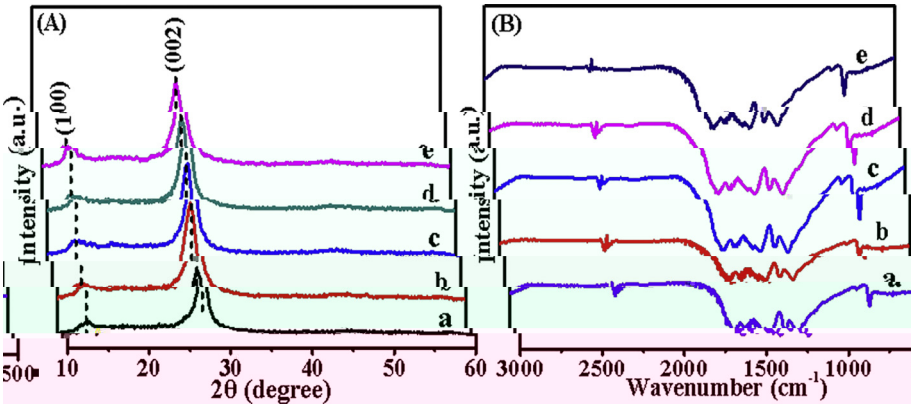

Fig. 1. (A) XRD and (B) FTIR patterns of (a) CNI, (b) CN/CNI-20%, (c) CN/CNI-40%, (d) CN/CNI-60% and (e) CN catalysts.

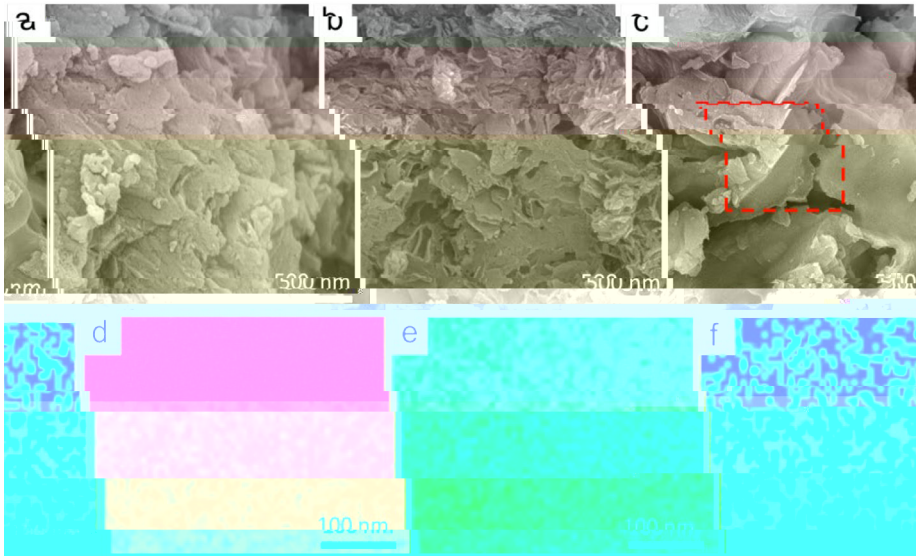

Fig. 2. SEM images of (a) CN, (b) CNI, (c) CN/CNI-40% and corresponding elemental mapping of (d) C, (e) N, (f) I in the CN/CNI-40% catalyst.

in CNI and CN/CNI-40% catalysts, indicating the successful formation of CN/CNI homojunction catalysts. The C 1 s XPS spectrum (Fig. 3A) could be deconvoluted into two peaks, the peak at 284.6 eV was attributed to carbon impurities, the peak at 288.2 eV was attributed to an sp^2-bonded carbon (C—C═N) [40]. The N 1 s XPS spectrum (Fig. 3B) could be deconvoluted into three peaks at 398.8, 399.7, and 401.1 eV, which were ascribed to sp^2-bonded nitrogen in N-containing aromatic rings (C—N═C), the tertiary nitrogen N-$(C)_3$ groups and the amino groups (C—N—H), respectively [41,42]. The I 3d XPS spectrum (Fig. 3C) could be deconvoluted into four peaks at 621.2, 621.9, 632.9, and 633.8 eV, corresponding to the I $3d_{5/2}$, I $3d_{5/2}$, I $3d_{3/2}$, I $3d_{3/2}$, respectively. The peaks at 621.2 and 621.9 eV were associated with the I^+, which were oxidation products of I^- during the reaction process [22]. However, in the CN/CNI-40% catalyst, the C 1 s peak binding energy (288.4 eV), the N 1 s peaks binding energy (398.9, 399.9, and 401.2 eV) and the I 3d peaks binding energy (621.4, 622.2, 633.2, and 634.0 eV) were respectively higher than that of the CN or CNI catalysts. This result not only confirmed the existence of iodine in the homojunction catalyst, but also reflected an intermolecular interaction between CN and CNI in their hybrid catalysts.

3.2. Activity and stability

The visible-light ($\lambda > 420$ nm) photocatalytic properties for degradation organic pollutant Rhodamine B (RhB) over the CN, CNI, CNI-R and CN/CNI catalysts were investigated, and the results were shown in Fig. 4A. Blank test in the lack of any catalyst was tested by same reaction conditions, which was barely decomposed without photocatalyst (only 4.5% removal) after being irradiated 4.0 h, indicating RhB direct photo-induced self-decomposition is negligible. The degradation ratio of CN, CNI, CNI-R was about 18%, 34%, 30% after 4.0 h, respectively. It was found that the synergetic effect of CN and CNI in their homojunction catalysts played a main role in improving catalytic efficiency. CN contents change from 20% to 60%, the activity of CN/CNI catalysts firstly increases, then decreased, and the highest photocatalytic activity was obtained by the CN/CNI-40% catalyst with the optimization content of CN, demonstrating that the combination of CN with CNI can exhibit superior catalytic activity towards RhB degradation. Furthermore, nearly 92% of RhB can be degraded by the CN/CNI-40% catalyst after an irradiation of 4.0 h, about 5.1, 2.7, 3.0 time as high as that of CN, CNI, CNI-R, respectively, confirming that CN/CNI-40% homojunction catalyst possesses an excellent property in degradation dye pollutants. The TOC removal efficiency was also studied (Fig. 4B), and the TOC removal efficiency was 35%, 44%, 47% and 71% for the CN, CNI-R, CNI and CN/CNI-40%, respectively, after 12 h photocatalytic reaction, indicating that massive intermediate products were oxidized and the CN/CNI-40% homojunction catalyst had excellent mineralizing ability.

The excellent photocatalytic H_2 evolution performance of CN, CNI, CNI-R and CN/CNI catalysts were evaluated (Fig. 5A), and CN, CNI and CNI-R shows a little activity, while the activity of CN/CNI homojunction

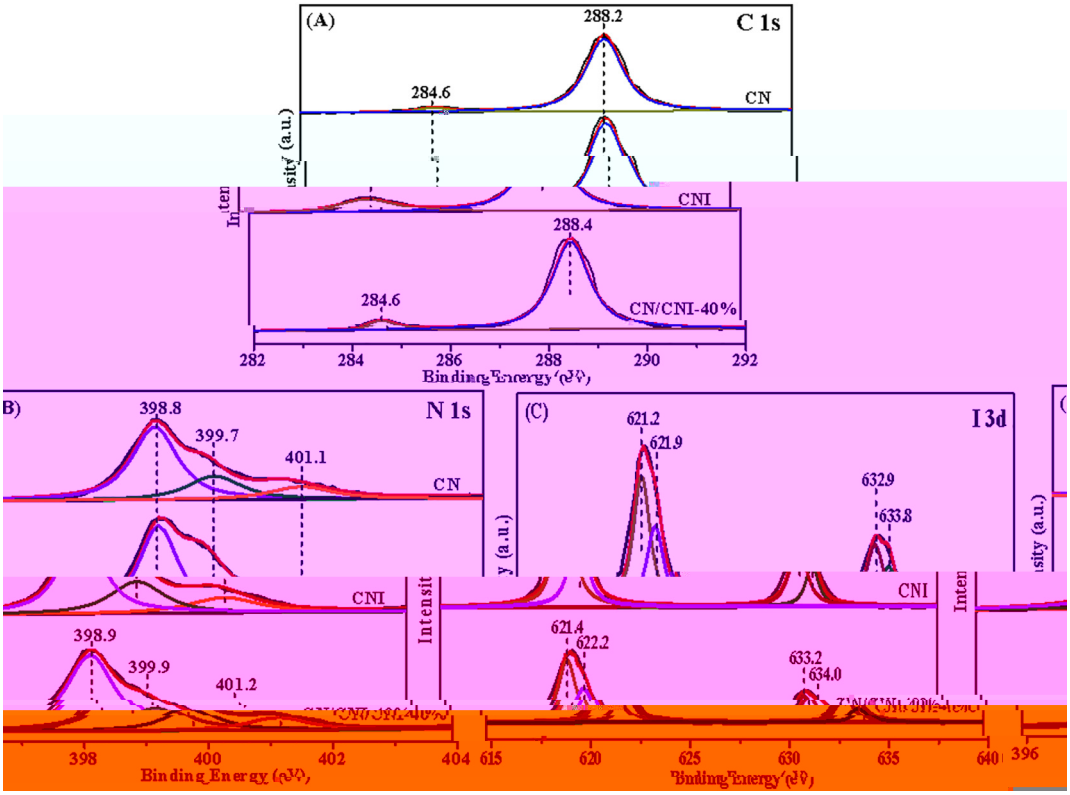

Fig. 3. XPS spectra of (A) C 1 s, (B) N 1 s and (C) I 3d peaks in CNI, CN/CNI-40% and CN catalysts.

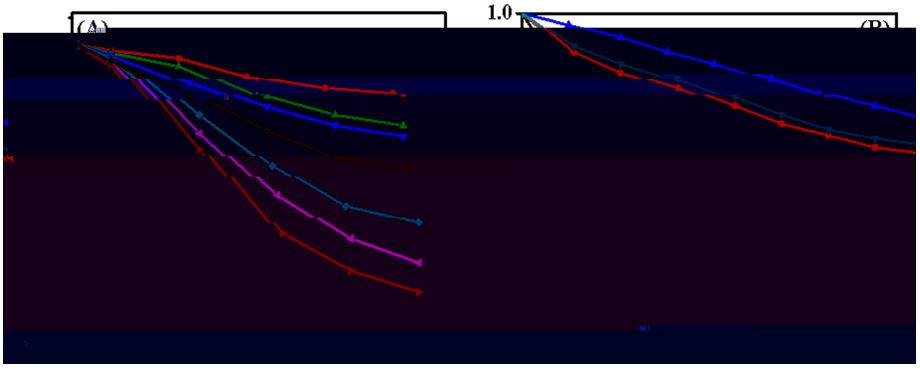

Fig. 4. (A) RhB degradation and (B) TOC removal for (a) blank, (b) CN, (c) CN/CNI-20%, (d) CN/CNI-40%, (d') CN/CNI-40% (physical mixture), (e) CN/CNI-60%, (f) CNI, (g) CNI-R catalysts under visible-light irradiation (λ > 420 nm).

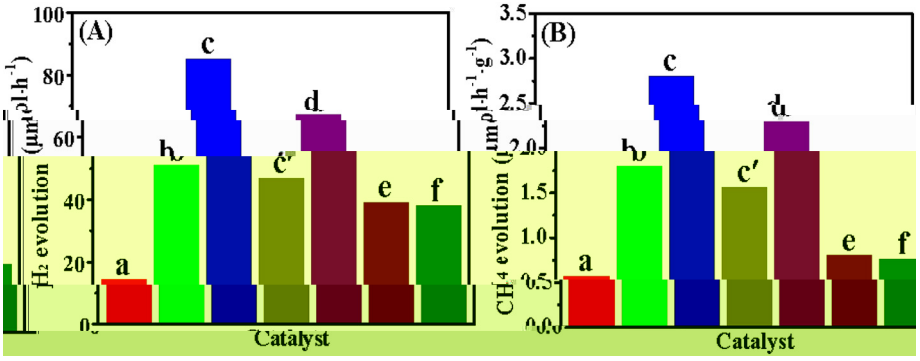

Fig. 5. (A) photocatalytic H_2 evolution rates and (B) photocatalytic CH_4 evolution rates for (a) CN, (b) CN/CNI-20%, (c) CN/CNI-40%, (c') CN/CNI-40% (physical mixture), (d) CN/CNI-60%, (e) CNI, and (f) CNI-R catalysts under visible-light irradiation (λ > 420 nm).

catalysts is significantly enhanced, further demonstrating the important role of homojunction. Also, we notice that the photocatalytic efficiency for H_2 evolution of CN/CNI catalysts follows the same order as photodegradation of RhB. Remarkably, the as-prepared CN/CNI-40% homojunction catalyst showed H_2 generation rate (85 $\mu mol \cdot h^{-1}$), which was 5.8, 2.1, 2.2 time higher than that of CN, CNI and CNI-R, respectively.

To further study the performance of CN/CNI homojunction catalysts, the reduction of CO_2 to CH_4 was also carried out (Fig. 5B). In comparison with CN, CNI, or CNI-R, all of the CN/CNI homojunction catalysts show significantly enhanced CO_2 reduction rates, with an order of CN < CNI-R < CNI < CN/CNI-20% < CN/CNI-60% < CN/CNI-40%. These results further lead us to conclude that the homojunction of CN/CNI is very important in improving the activity. Moreover, optimized CN/CNI-40% catalyst showed CO_2 reduction rate of 2.8 $\mu mol \cdot h^{-1} \cdot g^{-1}$, which was 4.9, 3.5, 3.6 time higher than that of CN, CNI, CNI-R, respectively. Notably, these results of the CN/CNI homojunction catalysts on the photoreduction CO_2 was in accordance with the photocatalytic degradation RhB and photocatalytic H_2 evolution in Fig. 4A and Fig. 5A.

Moreover, in order to further prove the role of homojunction of CN/CNI, the photocatalytic properties of physical mixture CN/CNI-40% were also tested (Figs. 4A and 5). RhB degradation ratio, H_2 production rate, CH_4 production rate of physical mixture CN/CNI-40% was obviously lower than that of the in-suit CN/CNI-40% homojunction catalyst, strongly suggesting that there was a synergistic effect between CN and CNI in the homojunction catalyst.

It is well known, stability of catalyst affects its application. Therefore, the photocatalytic repeatability was also evaluated by reusing the CN/CNI-40% homojunction catalyst (Fig. 6). After three cycles, there was no significant change in RhB degradation, H_2 evolution and CO_2 reduction over the CN/CNI-40% homojunction catalyst, implying that it has good stability.

3.3. Activity enhancement mechanism

The reasons of remarkably enhanced photocatalytic activity over the CN/CNI-40% homojunction catalyst are analyzed as follows. As we all know, the photocatalytic performance is usually influenced by the crystallinity, morphology, pore volume, specific surface area and band structure of catalysts. Compared with CNI, the specific surface area (Table 1), crystallinity (Fig. 1), pore volume (Table 1) and morphology (Fig. 2) of CN/CNI-40% showed a little change, implying that these factors were not keys for improving the activity. Therefore, visible-light absorption property, electron-hole separation of CN/CNI-40% might be two important factors for the improving catalytic property.

Table 1
Physicochemical properties of CN, CNI and CN/CNI catalysts.

Sample	Specific surface area (m^2/g)	Pore volume (cm^3/g)
CN	7	0.02
CNI	19	0.04
CN/CNI-20%	26	0.06
CN/CNI-40%	30	0.07
CN/CNI-60%	23	0.06

Optical properties for CN, CNI and CN/CNI catalysts were investigated (Fig. 7). Compared with CN or CNI, the CN/CNI catalysts extended a red shift and exhibited a stronger photo-absorption property in 442–591 nm regions, demonstrating the interaction between CN and CNI in the heterojunction may contribute to the narrowing of the band gap, which was contributed to the modified electronic structures of the photocatalyst matrix [10,26]. Meanwhile, the optical absorption properties and band gap structure of the CN/CNI homojunction catalysts could be very well controlled via tuning CN content. Furthermore, higher or lower CN content resulted in a lower absorption performance compared to that of CN/CNI-40% catalyst, implying that the suitable CN concentration will cause an optimized generation of charge carriers under light illumination and the interaction of CN and CNI could result in the strongest photoresponse among the CN/CNI as-synthesized catalysts.

The valence band X-ray photoelectron spectroscopy (VB XPS) was used to further research the influence of iodine-doped CN on positions of the valence band (VB). Fig. 8 showed VB XPS of CN and CNI catalysts. It can be known that the VB of CN and CNI was +1.78 eV, +1.53 eV, respectively. Combined with the Kubelka-Munk-transformed reflectance spectra (Fig. 7B), it can infer that the conduction band (CB) of CN and CNI was −0.92 eV, −1.13 eV, respectively. Obviously, CNI possessed a more negative CB compared to that of CN, indicating that CNI had a stronger reduction ability for photogenerated charge carriers [43].

Fig. 9 recorded the photoluminescence (PL) spectra of CN, CNI, CN/CNI-20% CN/CNI-40%, CN/CNI-60% catalysts. The three catalysts have a very strong similar emission band in the range of 400–600 nm, ascribed to the band-to-band transitions of CN [44,45]. The PL peaks of CN/CNI-20%, CN/CNI-40% and CN/CNI-60% weaken significantly in comparison with the CN or CNI. Among them, the PL peak of CN/CNI-40% was the weakest, implying that the recombination of charge carriers was greatly

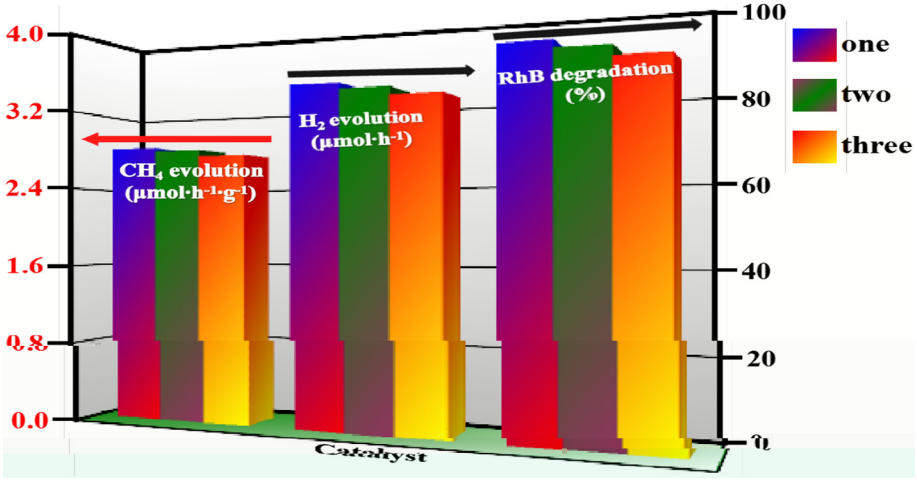

Fig. 6. Stability test of RhB degradation, H_2 evolution and CH_4 evolution for CN/CNI-40% recycling three times under visible-light irradiation ($\lambda > 420$ nm).

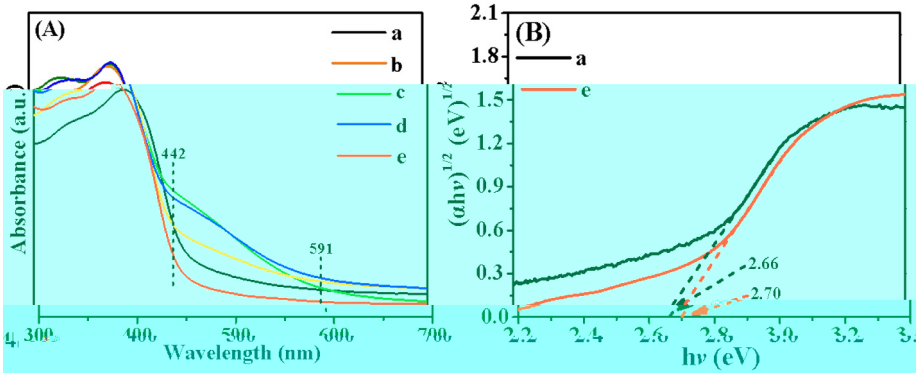

Fig. 7. (A) UV–Vis DRS and (B) Kubelka–Munk-transformed reflectance spectra of (a) CNI, (b) CN/CNI-20%, (c) CN/CNI-40%, (d) CN/CNI-60% and (e) CN catalysts.

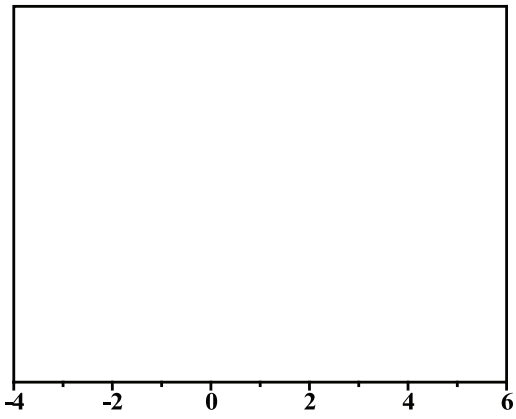

inhibited for CN/CNI-40% homojunction catalyst. This result suggested that the homojunction of CNI and CN can significantly improve the separation efficiency of electron-hole pairs, which is useful to improve the activities.

Electrochemical Impedance Spectroscopy (EIS) measurement is also an effective mean of investigating the resistance of charge transfer and the separation efficiency of photoinduced carriers. Fig. 10A showed EIS Nyquist plots for CN, CNI and CN/CNI-40% catalysts. It is well known that a smaller arc of an EIS Nyquist plot implies a smaller resistance of charge transfer on electrode surface [46]. Obviously, a decreased diameter of the EIS radius was observed for CN/CNI-40% compared to CN or CNI, showing a reduced electronic impedance and an improved charge mobility. In addition, transient photocurrent response measurements were carried out to further explore the transfer and separation of charge carriers. As shown in Fig. 10B, although CN, CNI and CN/CNI-40% catalysts showed a rapid response to light either off or on, the induced transient photocurrent density of CN/CNI-40% was 5.1, 1.9 time higher than that of CN or CNI, respectively. And the highest current density and smallest resistance of the CN/CNI-40% electrode verified the synergistic effect between the CN and CNI in the formation of homojunction catalyst. And the photocurrent is steady during five light-dark current cycles. Generally speaking, a higher photocurrent reflected a better separation ability of the photogenerated charges in the material [42]. Therefore, we can expressly figure out that the CN/CNI-40% illustrates an increased separation efficiency of the photoinduced carriers in homojunction catalyst as compared to individual CN and CNI.

Taken the above results and discussions together, we get a conclusion that the synergistic interaction between CN and CNI in their homojunction catalysts, especially for CN/CNI-40%, can result in an increased transfer and separation of interfacial charge carriers. Thus, enlarged light absorption property and accelerated separation/transport ability of photogenerated charges are mainly responsible for the enhanced reaction efficiency for CN/CNI catalysts.

Based on the above analysis, an activity enhancement proposed mechanism was presented for CN/CNI (Fig. 11). Photogenerated electrons-holes (Eq. (1)) of CN and CNI photocatalysts can be excited simultaneously by visible-light irradiation. According to theoretical calculation and previously reported results [47-49], there is a matching band structure between CN and CNI (Fig. 11). Due to the very well matched positions, CN/CNI homojunction could drive electron (e^-) migration from CNI to CN by conduction band offset, whereas the hole (h^+) can flow from CN to CNI by the valence band offset. As a result, electrons-hole pairs were effectively separated via using this technique, which was also supported by elevated photocurrent (Fig. 10B) and decreased photoluminescence intensity (Fig. 9) of CN/CNI. This causes an increase of photocatalytic performances over the CN/CNI catalysts.

However, the photocatalytic activities of CN/CNI homojunction catalysts have a close relationship with the composite proportion, and lower or higher CN concentration is inconvenient to increase the activity. With CN content increases from 20% to 40%, the CN/CNI catalysts produce a homogeneous dispersion process, which will promote the separation of electron-holes based on their matching electronic structure, thus resulting in enhanced catalytic performance. After that, excessive CN may block the active site on the CN/CNI contact interfaces and subsequently decrease the interfacial interaction of CN and CNI, causing a decreased photocatalytic activity. Therefore, the activity of CN/CNI

catalysts firstly increased and then decreased with increasing CN concentration, which results in the optimal photocatalytic performance of the CN/CNI-40% homojunction catalyst.

Catalyst + hv

between them can not only drive the e^- in CNI to transfer towards the CN, but also drive the h^+ in CN transfer towards the CNI by valence band offset. The h^+ would react with the surface-adsorbed water molecules or hydroxyl groups to form ·OH and $\cdot O_2^-$ radicals, along with H^+. Meanwhile, CO_2 would react with H^+ and e^- to produce CH_4 [53,54].

4. Conclusions

In summary, the novel CN/CNI homojunction catalysts were fabricated by a facile synthetic route. The optimized CN/CNI-40% catalyst with an appropriate CN content showed an excellent photocatalytic activity and stability, and its RhB degradation ratio, H_2 evolution rate, CO_2 reduction rate was 3.0, 2.2, 3.6 time higher than that of CNI-R (reference sample), respectively. The remarkably enhanced activity of CN/CNI-40% was mainly ascribed to the strengthened visible-light (442–591 nm) absorption performance and efficient separation of photogenerated carriers. Overall, these results indicated that highly efficient CN/CNI catalysts have great potentialities as a cheap multifunctional material applied in energy and environment fields in the near future.

Declaration of Competing Interest

None.

Acknowledgements

These works were financially supported via Major Research Project of National Natural Science Foundation from China (91643113), National Natural Science Foundation in China (21807012), Natural Science Foundation from Anhui Province in China (gxgwfx2018059, KJ2019A0513), Natural Science Research Projects of Fuyang Normal University of China (2017FSKJ09), Horizontal Cooperation Project of Fuyang municipal government and Fuyang Normal University (XDHX2016002, XDHX201711, XDHXPT201702, XDHX201716), Scientific Research Innovation Team of Fuyang Normal University (kytd201707) and Innovative training program for College Students (201810371023, 201810371041) in China.

References

[1] A. Dhakshinamoorthy, Z.H. Li, H. Garcia, Catalysis and photocatalysis by metal organic frameworks, Chem. Soc. Rev. 47 (2018) 8134–8172.

[2] R. Long, Y. Li, Y. Liu, S.M. Chen, X.S. Zheng, C. Gao, C.H. He, N.S. Chen, Z.M. Qi, L. Song, J. Jiang, J.F. Zhu, Y.J. Xiong, Isolation of cu atoms in Pd lattice: forming highly selective sites for photocatalytic conversion of CO_2 to CH_4, J. Am. Chem. Soc. 139 (2017) 4486–4492.

[3] X.J. Wen, C.G. Niu, L. Zhang, G.M. Zeng, Fabrication of SnO_2 nanopaticles/BiOI n–p heterostructure for wider spectrum visible-light photocatalytic degradation of antibiotic oxytetracycline hydrochloride, ACS Sustain. Chem. Eng. 5 (2017) 5134–5147.

[4] L. Tong, Z. Wang, C.X. Xia, Y.J. Yang, S.L. Yuan, D. Sun, X. Xin, Self-assembly of peptide-polyoxometalate hybrid sub-micrometer spheres for photocatalytic degradation of methylene blue, J. Phys. Chem. B 121 (2017) 10566–10573.

[5] S.Y. Zhu, S.J. Liang, J.H. Bi, M.H. Liu, L.M. Zhou, L. Wu, X.X. Wang, Photocatalytic reduction of CO_2 with H_2O to CH_4 over ultrathin $SnNb_2O_6$ 2D nanosheets under visible light irradiation, Green Chem. 18 (2016) 1355–1363.

[6] L.F. Gao, T. Wen, J.Y. Xu, X.P. Zhai, M. Zhao, G.W. Hu, P. Chen, Q. Wang, H.L. Zhang, Iron-doped carbon nitride-type polymers as homogeneous organocatalysts for visible light-driven hydrogen evolution, ACS Appl. Mater. Interfaces 8 (2016) 617–624.

[7] D.T. Zhang, T.Y. Xu, M.Y. Cao, A.J. Liu, Q. Zhao, L. Zhang, H.Y. Zhang, T.Y. Xue, X.Q. Cui, W.T. Zheng, Facile band alignment of C_3N_4/CdS/MoS_2 sandwich hybrid for effifi

[37] J.N. Liu, Q.H. Jia, J.L. Long, X.X. Wang, Z.W. Gao, Q. Gu, Amorphous NiO as co-catalyst for enhanced visible-light-driven hydrogen generation over g-C_3N_4 photocatalyst, Appl. Catal. B Environ. 222 (2018) 35–43.
[38] Z.Y. Wang, M.J. Chen, Y. Huang, X.J. Shi, Y.F. Zhang, T.T. Huang, J.J. Cao, W.K. Ho, S.C. Lee, Self-assembly synthesis of boron-doped graphitic carbon nitride hollow tubes for enhanced photocatalytic NOx removal under visible light, Appl. Catal. B Environ. 239 (2018) 352–361.
[39] T.Y. Ma, Y.H. Tang, S. Dai, S.Z. Qiao, Proton-functionalized two-dimensional graphitic carbon nitride nanosheet: an excellent metal−/label-free biosensing platform, Small 10 (2014) 2382–2389.
[40] Z.Z. Lin, X.C. Wang, Nanostructure engineering and doping of conjugated carbon nitride semiconductors for hydrogen photosynthesis, Angew. Chem. Int. Ed. 52 (2013) 1735–1738.
[41] S.X. Hua, D. Qu, L. An, W.S. Jiang, Y.J. Wen, X.Y. Wang, Z.C. Sun, Highly efficient p-type Cu_3P/n-type g-C_3N_4 photocatalyst through Z-scheme charge transfer route, Appl. Catal. B Environ. 240 (2019) 253–261.
[42] M.Y. Huang, Y.L. Zhao, W. Xiong, S.V. Kershaw, Y.G. Yu, W. Li, T. Dudka, R.Q. Zhang, Collaborative enhancement of photon harvesting and charge carrier dynamics in carbon nitride photoelectrode, Appl. Catal. B Environ. 237 (2018) 783–790.
[43] P.F. Xia, B.C. Zhu, J.G. Yu, S.W. Cao, M. Jaronie, Ultra-thin nanosheet assemblies of graphitic carbon nitride for enhanced photocatalytic CO_2 reduction, J. Mater. Chem. A 5 (2017) 3230–3238.
[44] Q. Li, N. Zhang, Y. Yang, G.Z. Wang, D.H.L. Ng, High efficiency photocatalysis for pollutant degradation with MoS_2/C_3N_4 heterostructures, Langmuir 30 (2014) 8965–8972.
[45] J.W. Fu, J.G. Yu, C.J. Jiang, B. Cheng, g-C_3N_4-Based heterostructured photocatalysts, Adv. Energy Mater. 8 (2018) 1701503.
[46] B. Wang, S. He, L.L. Zhang, X.Y. Huang, F. Gao, W.H. Feng, P. Liu, CdS nanorods decorated with inexpensive NiCd bimetallic nanoparticles as efficient photocatalysts for visible-light-driven photocatalytic hydrogen evolution, Appl. Catal. B Environ. 243 (2019) 229–235.
[47] Y.N. Wang, Y.Q. Zeng, S.P. Wan, W. Cai, F.J. Song, S.L. Zhang, Q. Zhong, In situ fabrication of 3D octahedral g-C_3N_4/$BiFeWO_x$ double-heterojunction for highly selective CO_2 photoreduction to CO under visible light, ChemCatChem 10 (2018) 4578–4585.
[48] S.W. Cao, B.J. Shen, T. Tong, J.W. Fu, J.G. Yu, 2D/2D heterojunction of ultrathin MXene/Bi_2WO_6 nanosheets for improved photocatalytic CO_2 reduction, Adv. Funct. Mater. 28 (2018) 1800136.
[49] D.F. Xu, B. Cheng, W.K. Wang, C.J. Jiang, J.G. Yu, Ag_2CrO_4/g-C_3N_4/graphene oxide ternary nanocomposite Z-scheme photocatalyst with enhanced CO_2 reduction activity, Appl. Catal. B Environ. 231 (2018) 368–380.
[50] Y. Imada, Y. Okada, K. Noguchi, K. Chiba, Selective functionalization of styrenes with oxygen using different electrode materials: olefin cleavage and synthesis of tetrahydrofuran derivatives, Angew. Chem. Int. Ed. 58 (2019) 125–129.
[51] Y. Zeng, N. Guo, H.Y. Li, Q.Y. Wang, X.J. Xu, Y. Yu, X.R. Han, H.W. Yu, A novel route to manufacture WO_3@MoS_2 p–n heterostructure hollow tubes with enhanced photocatalytic activity, Chem. Commun. 55 (2019) 683–686.
[52] W.Y. Lu, T.F. Xu, Y. Wang, H.G. Hu, N. Li, X.M. Jiang, W.X. Chen, Synergistic photocatalytic properties and mechanism of g-C_3N_4 coupled with zinc phthalocyanine catalyst under visible light irradiation, Appl. Catal. B Environ. 180 (2016) 20–28.
[53] Q. Li, S.C. Wang, Z.X. Sun, Q.J. Tang, Y.Q. Liu, L.Z. Wang, H.Q. Wang, Z.B. Wu, Enhanced CH_4 selectivity in CO_2 photocatalytic reduction over carbon quantum dots decorated and oxygen doping g-C_3N_4, Nano Res. 12 (2019) 2749–2759.
[54] R.A. Rather, M. Khan, I.M.C. Lo, High charge transfer response of g-C_3N_4/ag/AgCl/$BiVO_4$ microstructure for the selective photocatalytic reduction of CO_2 to CH_4 under alkali activation, J. Catal. 366 (2018) 28–36.